Microchimica Acta
https://doi.org/10.1007/s00604-019-3479-5

ORIGINAL PAPER

A bimetallic (Cu-Co) Prussian Blue analogue loaded with gold nanoparticles for impedimetric aptasensing of ochratoxin a

Chenxi Gu[1] · Longyu Yang[2] · Minghua Wang[2] · Nan Zhou[1] · Linghao He[2] · Zhihong Zhang[2] · Miao Du[2]

Received: 22 March 2019 / Accepted: 30 April 2019

Abstract

Bimetallic (Cu-Co) Prussian Blue analogs (PBAs) were coupled to gold nanoparticles to give a nanocomposite of type AuNP@CuCoPBA. It is shown to be a viable material for the impedimetric aptamer-based determination of ochratoxin A (OTA). Basic characterizations revealed that the chemical composition and crystal structure of AuNP@CuCoPBA is similar to that of pristine CuCo PBA. Nevertheless, the nanocube shape of CoCu PBA is converted to small nanoparticles on addition of AuNPs. Compared with CuCoPBA-based aptasensor, the AuNP@CuCoPBA-based assay exhibits excellent electrochemical conductivity, strong aptamer binding interaction, and high G-quadruplex stability. Electrochemical impedance spectroscopy revealed that the assay has limits of detection as low as 5.2 fg mL^{-1} of OTA, a response in the 50 fg mL^{-1} to 10 ng mL^{-1} concentration range, high selectivity, good reproducibility, repeatability, and acceptable applicability. In our perception, it represents a universal and powerful method for aptamer strand immobilization. It may be applied to the determination of various other analytes for which aptamers are available.

Keywords Detection of mycotoxins · Electrochemical biosensor · Metal-organic frameworks · Nanocomposites · Food safety testing

Introduction

Ochratoxin A (OTA) is one of the prevalent mycotoxins contaminating food. It can be present in food like rice, peanut, coffee, and maize, further entering animals' bodies, invading human blood and breast milk through the food chain. OTA mainly affects the kidney and liver in both humans and animals, exerting nephrotoxic, carcinogenic, hepatotoxic and immunotoxic effects on most mammalian species [1]. The United Nations Cancer Research Organization placed OTA as class 2B carcinogen; The European Commission has established the maximum level of OTA in several food products, including cereals (3.0 ng·g^{-1}), raw cereal grains (5.0 ng·g^{-1}), dried fruits (10.0 ng·g^{-1}), wine and grape juice (2.0 ng·g^{-1}) [2]. Therefore, it is of great importance to develop some rapid, sensitive and convenient method to detect OTA in the fields of food safety. At moment, conventional methods for toxins analysis are usually focused on the public accepted methods of mass spectrometry, high-performance liquid chromatography, and gas chromatography enzyme-linked immunosorbent assay, along with other analytical methods, such as surface enhanced Raman scattering, electrochemiluminescence, fluorescence assay, and colorimetric assay [3]. Nevertheless, their widespread usage is limited by the requirement of specially trained personnel and sophisticated equipment, which are definitely hard to meet the current requirements of in-situ and rapid determination. Electrochemical assays based on biosensor have been widely studied for the detection of OTA because its

Electronic supplementary material The online version of this article (https://doi.org/10.1007/s00604-019-3479-5) contains supplementary material, which is available to authorized users.

✉ Nan Zhou
fcczhoun@zzu.edu.cn

✉ Zhihong Zhang
mainzhh@163.com

✉ Miao Du
dumiao@zzuli.edu.cn

[1] Department of Orthopedics, The First Affiliated Hospital of Zhengzhou University, No. 1, Jianshe East Road, Zhengzhou 450052, China

[2] Henan Provincial Key Laboratory of Surface and Interface Science, Zhengzhou University of Light Industry, No. 136, Science Avenue, Zhengzhou 450001, People's Republic of China

Published online: 10 May 2019

equipment is inexpensive and simple, and easy to realize miniaturization [4].

Aptamers, single-stranded DNA/RNA strands designed through an in vitro selection technique known as systematic evolution of ligands by exponential enrichment and can bind to specific molecules, have attracted increased attention in biosensor fields due to their good specificity, high stability, nontoxicity, flexible design, small size, low cost, and simplicity [5]. Electrochemical aptamer sensors (aptasensors) have been developed by immobilizing an aptamer on an electrically conducting substrate, which is typically a carbon-based or Au electrode in various applications. As aforementioned, the key step in developing a performing aptasensor involves aptamer immobilization on the transducer surface. Normally, aptamer strands were often modified with thiol group, biotin, amino, or azide group in order to bind with the substrate through various covalent bonds [6]. Moreover, additional electroactive labels, such as methylene blue, ferrocene derivatives, and ruthenium complexes, have also been used for labeling aptamer and monitoring the electrochemical signal [7]. These approaches undoubtedly lead to the cost increase in the fabrication of aptasensors. Hence, seeking advanced transducer materials is a feasible way to develop label-free electrochemical aptasensors with ultralow sensitivity and high selectivity, because they can act as a support for increasing aptamer loading, connecting the aptamers to electrodes through conducting nanomaterials, and providing a higher electroactive area [8]. The development of nanomaterials brought up significant progress with regard to sensitive electrochemical detection, stable aptamer immobilization, and efficient aptamer-based sensing schemes.

As a member of the family of metal-organic frameworks, Prussian Blue (PB) and Prussian Blue analogues (PBAs) have received intensive investigation in the fields of catalysis, sensing, batteries, gas storage and separation, drug delivery, molecular magnetism, and photomagnetism [9]. Given their diverse morphologies, good electrocatalytic activity and stability, low cost, and uniform and easily controllable sizes, nanostructured PB/PBA materials and their derivatives have been used to construct various sensors for detecting molecules, such as ascorbic acid, hydrazine, antibiotics, heavy metal ions, pesticide, and volatile organic compounds [10]. However, their poor electroactivity and low instability in neutral and alkaline solutions of most PBs limit their applications in sensing fields. Designing advanced label-free aptasensors based on PBAs with excellent conductivity and high sensitivity is necessary to conduct further investigation. Metal nanoparticles (NPs, Au NPs and Ag NPs) and carbon materials (carbon nanotubes and graphene) can significantly increase the electrical conductivity, affinity, and biocompatibility of PBA nanomaterials. For instance, a triple-component of graphite felt, Ag NPs and PB was fabricated for the highly sensitive detection of hydrazine. The π-conjugated structure of nitrogen-doped graphene quantum dots provides an excellent platform for aptamer immobilization through π-π stacking interaction, giving a detection limit of 3.1 nM for detecting chloramphenicol antibiotic [11]. Multi-walled carbon nanotubes decorated with PB nanocube composite exhibited high sensitivity and selectivity for the simultaneous detection of sulfamethoxazole (SMX) and trimethoprim (TMP) antibiotics, with limit of detection (LOD) of 38 and 60 nM for SMX and TMP, respectively [12]. Howbeit, most of PB-based sensing transducer materials only consist of sole metal center. Bimetallic PBAs and their derivatives, which displayed different oxidation states of metal ions and vacancies for balancing charges, exhibited superior properties on the basis of synergetic effect among the different metal counterparts [13]. In our previous work, bimetallic NiFe PBA-derived NiO_xFeO_y@mC composite was used as a sensing scaffold for the detection of adenosine triphosphate. And good electrochemical sensing performances were obtained only after the calcination of NiFe PBA at high temperature [14]. Nevertheless, the calcination treatment toward bimetallic PBAs can overcome this shortcoming to a certain extent, tedious calcination procedure and high energy and time consumption limit their application in the biosensing fields. Although couples of bimetallic PBAs or their derivatives have already been exploited as the bioplatform for the aptasensor construction, poor electrochemical performances and weak binding force of the G-quadruplex between aptamer strands and analytes lead to low detection ability. Consequently, feasible construction of PB- or PBA-based aptasensors is still in the early stage.

More recent spectroscopic and structural evidence show that the building block vacancies ($[Mn(CN)_6]_{n-6,}$ where M = Co, Ni, Mn, Fe) can be present in both ordered and/or disordered states [9]. Specifically, PBA nanocube precursors containing nickel, cobalt, and iron were utilized to maintain general nanocuboidal structure while optimizing the composition of transition metal centers to efficiently bind the biomolecules. Additionally, as one of the most studied nanomaterials, Au NPs possess a variety of useful features, including size tunability, simple synthesis and monodispersity in aqueous buffer [15]. Considering the advantages of PBA and Au NPs, we aim to synthesize a new nanocomposite of bimetallic CoCu PBA coupling with Au NPs (**Step ii**, Scheme 1) and explore it as the platform for a novel aptasensor to detect OTA by electrochemical techniques (Scheme 1). The presence of AuNPs can enhance the electrochemical activity of PBA, whereas the PBA matrix can supply more cavities to adsorb large amounts of aptamer strands and analytes. When the OTA aptamer strand immobilizes over the AuNP@CuCoPBA-based nanocomposites through electrostatic interaction between the positive charged N [16] (**Step ii**, Scheme 1), OTA molecules can be successfully recognized by specific OTA/aptamer binding event [17]. The aptamer changes from a single strand to a G-

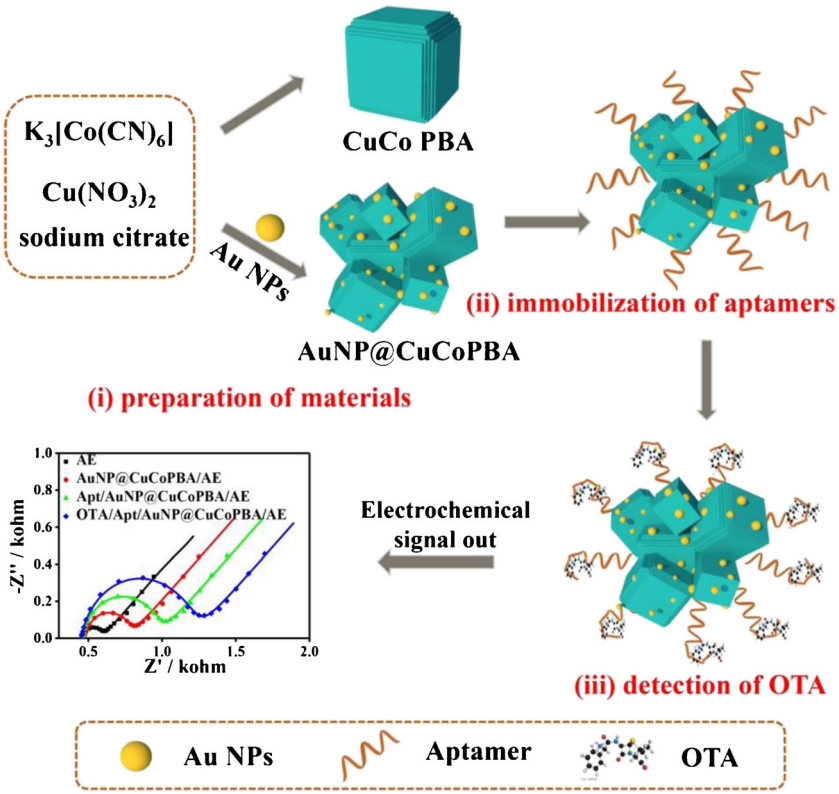

Scheme 1 Schematic diagram of the aptasensor fabrication based on the series of CoCu PBA, including (i) preparation of the CuCo PBA, and AuNP@CuCoPBA, (ii) immobilization of the aptamer strands, and (iii) detection of OTA

quadruplex structure, which was demonstrated previously using circular dichroism spectroscopy [18], and results in an electrochemical signal change. (**Step iii**, Scheme 1). Each step of the aptasensor fabrication and analyte detection can be determined by electrochemical techniques. In comparison with the pristine CuCoPBA-based aptasensor, the AuNP@CuCoPBA-based sensing system exhibits the superior detection efficiency toward OTA, together with ultrasensitivity, high selectivity, good stability, and an extremely limitation of detection (LOD) of 5.2 fg mL^{-1}. We believe that this kind of sensing platform would have great and wide potential applications in the fields of food safety and environmental monitoring.

Experimental section

The parts of chemicals and regents, solution preparation, synthesis of CuCo PBA, characterizations, and electrochemical measurements were provided in the **Electronic Supplementary Material** (**ESM**).

Synthesis of the AuNP@CuCoPBA composite

As for the preparation of AuNP@CuCoPBA, 0.133 g of $K_3[Co(CN)_6]$ and 0.145 g of $Cu(NO_3)_2$ were dissolved in 15 mL of Milli-Q water to obtain Solution **A**, whereas 0.265 g of sodium citrate was dissolved in Milli-Q water to obtain Solution **B**. Afterward, Solution **A** was added into Solution **B**. Then, 2 mL of $HAuCl_4 \cdot 3H_2O$ (0.1 mg·mL^{-1}) was added in the mixed solution under magnetic stirring. The mixture solution was aged for 24 h at room temperature. The resultant precipitate was collected by centrifuging at 8000 rpm for 5 min, following by washing with water for several times, and drying under vacuum at 60 °C for 6 h. Finally, the AuNP@CuCoPBA powder was obtained.

Fabrication of the AuNP@CuCoPBA-based aptasensor

The bare gold electrode (AE) (3 mm diameter, 7.065 mm^2) was polished into a smooth surface by using 0.05 μm alumina powder and ultrasonically washed in piranha solution (a concentrated sulfuric acid and hydrogen peroxide mixture, H_2SO_4:H_2O_2 = 7:3, *v*/*v*) for 15 min. Afterward, the bare AE was electrochemically cleaned through oxidation and reduction cycling in 0.5 M H_2SO_4 from −0.2 V to 1.6 V (vs. Ag/AgCl), rinsed with Milli-Q water, and dried under nitrogen. The CuCo PBA and AuNP@CuCoPBA (10 mg) were separately dispersed in 10 mL of Milli-Q water to obtain homogeneous dispersions with concentration of 1.0 mg mL^{-1}.

Taking the construction of the AuNP@CuCoPBA-based aptasensor as an example, the dispersion of AuNP@CuCoPBA (5 μL) was dropped onto the pre-treated AE surface and dried at room temperature (represented by AuNP@CuCoPBA/AE). Subsequently, the AuNP@CuCoPBA/AE was immersed in the aptamer solution

(100 nM) for 30 min to ensure that the aptamer strand was immobilized over the electrode surface until saturation (represented by Apt/AuNP@CuCoPBA/AE). The used OTA aptamer strand is composed of the sequence of 5′-TTT TTG ATC GGG TGT GGG TGG CGT AAA GGG AGC ATC GGA CA-3′. Finally, the Apt/AuNP@CuCoPBA/AE was immersed in the OTA solution with different concentrations for further measurements (represented by OTA/Apt/AuNP@CuCoPBA/AE). Similarly, the CuCoPBA-based aptasensor was constructed using the same procedure. All the electrochemical measurements, including electrochemical impedance (EIS) and cyclic voltammetry (CV) were carried out on the CHI660D electrochemical workstation (Shanghai Chenhua, China). The detailed description of the electrochemical measurements, EIS Nyquist plots, and equivalent circuit (**Fig. S1**) was supplied in **ESM**.

For the applicability test, the fresh watermelon was squeezed out of the juice, following by being filtered with a filter of 0.22 μm. Afterward, the watermelon juice was diluted 200 times with 0.01 M PBS. The diluted watermelon juice was spiked with OTA with different concentrations.

Results and discussion

Crystal and chemical structures of the CuCo PBA and AuNP@CuCoPBA nanospheres

The XRD characterizations of all samples were displayed in **Fig. S2a**, while the relevant discussion was supplied in **ESM**. The chemical structures of CuCo PBA and AuNP@CuCoPBA were further confirmed by FTIR (**Fig. S2b**). FTIR spectra show a sharp peak at about 2185 cm^{-1}, which is assigned to the stretching vibration peak of the bridging cyano group (-CN). The bands at 3420 and 1610 cm^{-1} are respectively attributed to the O-H stretching vibration and O-H bending vibrations of the crystal water in the framework. Moreover, the detailed chemical structure and components of CuCo PBA and AuNP@CuCoPBA were also characterized by XPS, of which the Cu 2*p*, Co 2*p*, C 1 *s*, N 1 *s*, and O 1 *s* signals are observed in their XPS survey spectra (**Fig. S2c**). To evaluate the chemical valence and environments of each element containing in CuCo PBA and AuNP@CuCoPBA, the high-resolution XPS spectra of Cu 2*p*, Co 2*p*, C 1 *s*, and N 1 *s* were analyzed, as displayed in Fig. 1a-d. The high-resolution XPS spectrum of Cu 2*p* can be deconvulated into the peaks at the binding energies of 932. 5 and 952.9 eV (Fig. 1a), due to the Cu $2p_{3/2}$ and Cu $2p_{1/2}$ of Cu(I), respectively, along with the peaks at the BEs of 935.9 and 955.6 eV, which are due to the Cu $2p_{3/2}$ and Cu $2p_{1/2}$ of Cu(II), respectively. Additionally, the characteristic satellite peaks at the BEs at 963–962 and 943–942 eV are also appeared. The fitted curve of the high-resolution Co 2*p* XPS spectrum is demonstrated in Fig. 1b. The peaks at the BEs of 778.8 eV and 781.9 eV are assigned to the metallic Co, Co(0), and Co(II) of Co $2p_{3/2}$, whereas the peaks at the BEs of 795 and 797 eV are attributed to Co(0) and Co(II) of Co $2p_{1/2}$, respectively. The other peak at the BE of 798.9 eV is the satellite peak of Co(I). As for the high-resolution C 1 *s* XPS spectrum, three main peaks at the BEs of 284.5, 285.3, and 286.3 eV (Fig. 1c) are corresponded to

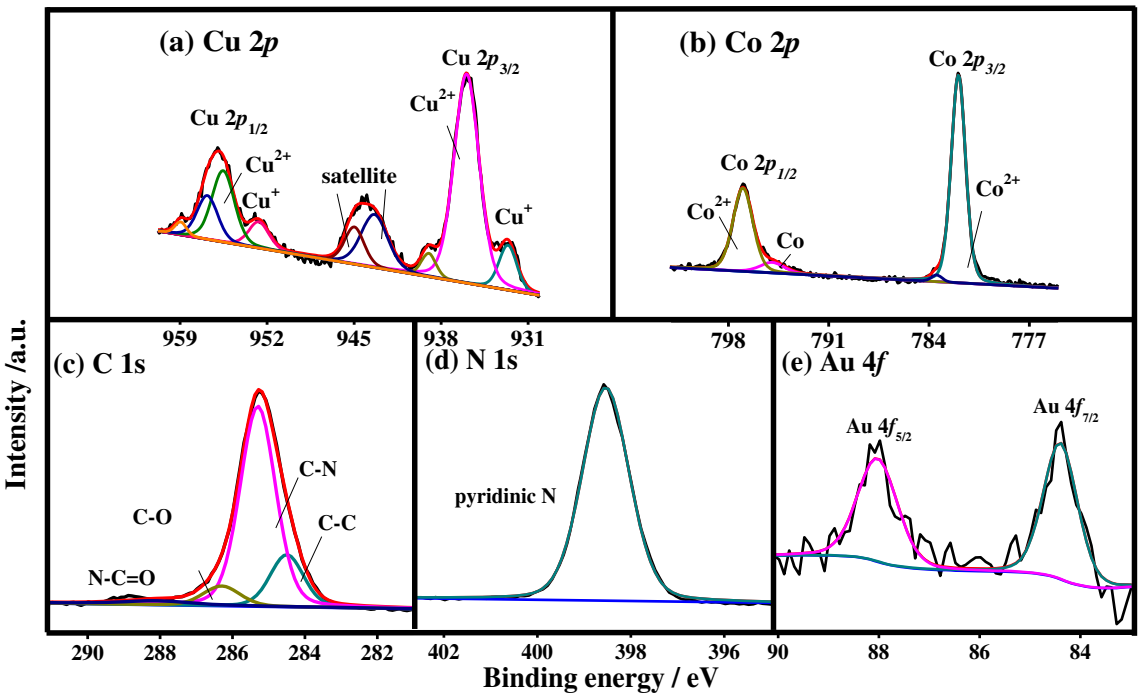

Fig. 1 **a** Cu 2*p*, **b** Co 2*p*, **c** C 1 *s*, **d** N 1 *s*, and **e** Au 4*f* core-level XPS spectra of AuNP@CuCoPBA

the C-C, C-N, and C-O, respectively, whereas a weak peak at the BE of 289 eV is assigned with the N-C=O group. Only one main peak at the BE of 398.6 eV is observed in the high-resolution N 1 *s* XPS spectrum (Fig. 1d), which is due to the pyridine N binding. Furthermore, the high-resolution XPS spectra of Cu 2*p*, Co 2*p*, C 1 *s*, and N 1 *s* containing in the pristine CuCo PBA were also analyzed, as illustrated in **Fig. S3**. The similar analyzed results are obtained, hinting that the chemical environment of each element is same. Additionally, as for the AuNP@CuCoPBA nanospheres, a clear Au 4*f* signal is deconvulated into two doublets, corresponding to Au $4f_{7/2}$ and Au $4f_{5/2}$ spin-orbit components at the BEs of 84.4 and 88 eV, respectively (Fig. 1e). The Au $4f_{7/2}$ component at the BEs of 83.0 and 84.3 eV are assigned to metallic Au and the second to oxidized surface species Au^{3+} species, respectively [19]. This result further confirms that the combination of Au NPs with the CuCo PBA nanospheres.

Surface morphologies of the CuCo PBA and AuNP@CuCoPBA nanospheres

Surface morphologies and nanostructures of the CuCo PBA and AuNP@CuCoPBA were characterized by FE-SEM and TEM. As shown in **Fig. S4a**, CuCo PBA nanospheres are highly uniform with a size ranging from 700 nm to 1 μm. The single-crystal-like characteristic of the CuCo PBA nanospheres was confirmed by its FE-SEM image (**Fig. S4b**), showing a very smooth surface. Each face is composed of several layers with different sizes, which also can be proven by its TEM images (**Figs. S4c** and **S4d**). When combined with Au NPs, the surface morphology of AuNP@CuCoPBA is changed from nanospheres to NPs with a size of 50 nm (Fig. 2a and b**)**. From the TEM image of AuNP@CuCoPBA (Fig. 2c), abundant Au NPs were embedded within the CuCo PBA cavities. A representative high-resolution TEM image (Fig. 2d) reveals that the (200) lattice spacing (0.201 nm) and the (222) lattice spacing (0.117 nm) can be clearly observed, which are attributed to the face centered cubic Au [20]. This finding indicates that Au NPs were uniformly dispersed into the CuCo PBA matrix. All of these results suggest the successful combination of Au NPs with CoCu PBA nanospheres.

Electrochemical biosensing performances of the CuCoPBA- and AuNP@CuCoPBA -based aptasensors

For comparison, CuCo PBA and AuNP@CuCoPBA nanospheres were concurrently used as platforms for immobilizing aptamer strands to construct the OTA-targeted aptasensor. The whole determination procedures for the detection of OTA using two kinds of aptasensors were investigated by EIS (Fig. 3) and CV (**Fig. S5**). The R_{ct} values was calculated using an equivalent circuit model (inset of **Fig. S1**), while they were summarized in **Table S1**. In terms of the AuNP@CuCoPBA-based aptasensor (Fig. 3a), the bare AE exhibits a low R_{ct} value of 0.135 kohm, hinting its excellent electrochemical conductivity and low electron transfer resistance. As the AE

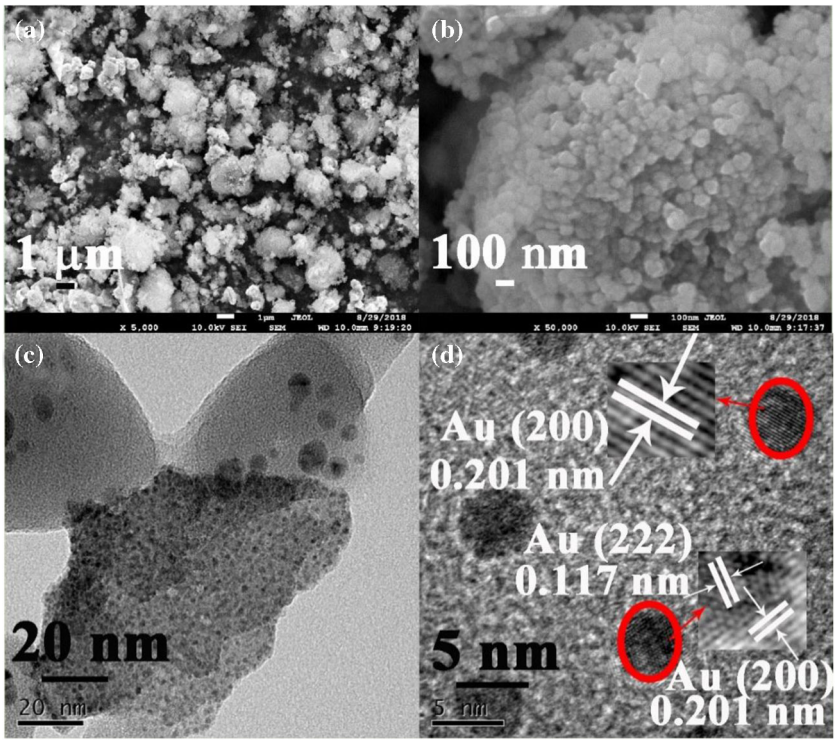

Fig. 2 **a**, **b** Low- and high-magnitude SEM images, and **c**, **d** TEM and HR-TEM images of AuNP@CuCoPBA

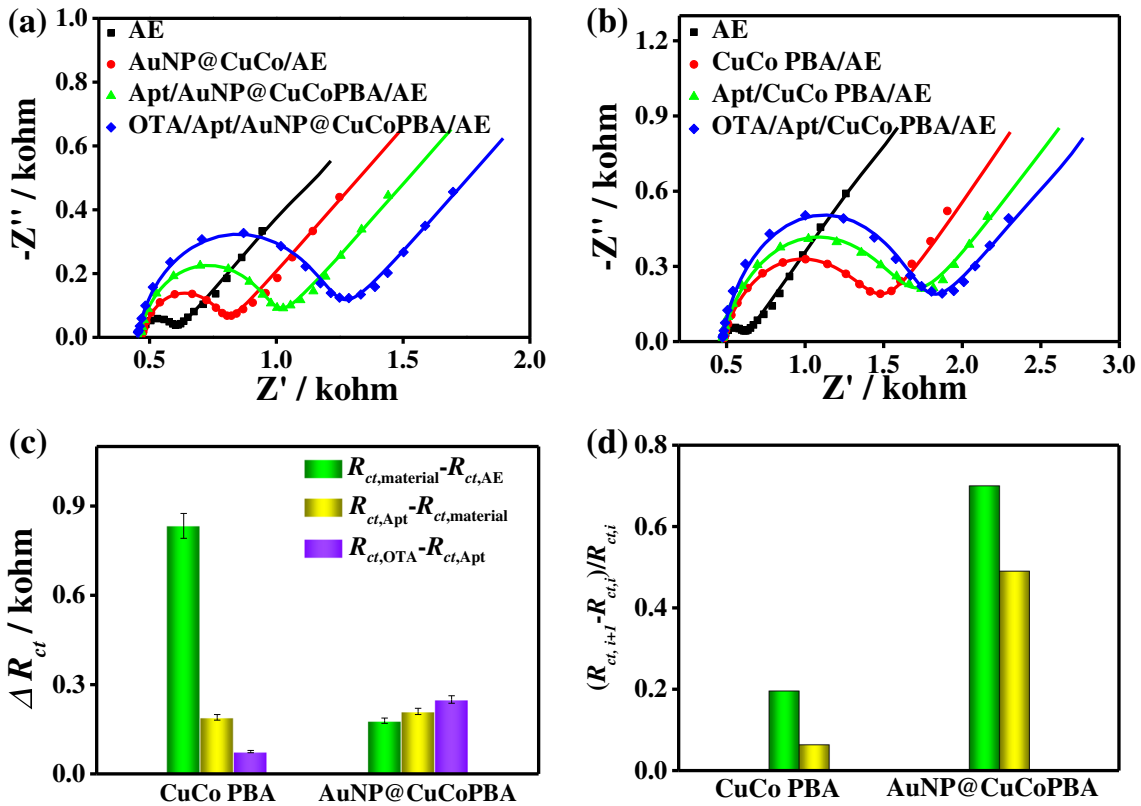

Fig. 3 EIS Nyquist plots of the determination procedure for OTA by (**a**) AuNP@CuCoPBA-, and (**b**) CuCo PBA-based aptasensor (including the bare AE, Materials/AE, Apt/Materials/AE, and OTA/Apt/Materials/AE). (**c**) ΔR_{ct} values at each stage for the OTA detection using the fabricated aptasensors based on the pristine CuCo PBA and AuNP@CuCoPBA. (**d**) The relative change of the R_{ct} values $[(R_{ct,\,i+1}\text{-}R_{ct,i})/R_{ct,i}]$ for the aptamer immobilization and OTA detection using the aptasensors based on the pristine CuCo PBA and AuNP@CuCoPBA composites in 0.1 M PBS (pH 7.4) containing 5.0 mM $[Fe(CN)_6]^{3-/4-}$ redox

was modified with the AuNP@CuCoPBA nanospheres, the R_{ct} value of the AuNP@CuCoPBA/AE slightly increases to 0.30 kohm, indicating the AuNP@CuCoPBA possesses poorer electrochemical conductivity than that of the bare AE, further hampering electron from transferring at the interface between the electrode surface and the electrolyte solution [5]. Compared with other PBA nanomaterials, howbeit, the AuNP@CuCoPBA displays enhanced electrochemical conductivity, indicating that Au NPs can facilitate the electron transfer at the interface between nanomaterial and electrolyte solution. When immobilizing aptamer strands (100 nM) onto the AuNP@CuCoPBA/AE, the large R_{ct} value (0.51 kohm) is obtained. Owning to large amounts of negative-charged phosphate groups contained in the introduced aptamer, the repulsion force is happened with $[Fe(CN)_6]^{3-/4-}$, further prevent the electron from transferring to the electrode surface [21]. Moreover, the EIS Nyquist plots obtained from the kinetics behavior of the Apt/AuNP@CuCoPBA/AE in the electrolyte solution indicated the good stability of the aptamer strands over the electrode (**Fig. S6**). As the AuNP@CuCoPBA-based aptasensor was used to determine OTA (0.5 pg mL^{-1}), the R_{ct} value continuously increases to 0.76 kohm due to the captured OTA molecules on the sensor interface as a blocking layer, further impeding the mass transfer and electron transfer on the electrode surface [22]. Similarly, the CuCoPBA-based aptasensor was also fabricated to detect OTA (Fig. 3b). The same trends of electrochemical performances during the detection procedure for two samples were observed. As for the CuCoPBA-based aptasensor, the R_{ct} values of each step increases with the order of the electrode modification, aptamer immobilization, and OTA detection, i.e., 0.132, 0.97, 1.16, and 1.23 kohm, respectively. A larger R_{ct} value of CuCoPBA-modified AE reveals its substantially low electrochemical conductivity in comparison with the AuNP@CuCoPBA/AE.

Nevertheless, evaluating the detection efficiency toward OTA only from these electrochemical results is not very feasible. A newly credible technique should be constructed. To investigate the difference in the OTA detection using various aptasensors based on the CuCo PBA and AuNP@CuCoPBA, their corresponding ΔR_{ct} values for each step during detection procedures are calculated, as displayed in Fig. 3c. The difference in R_{ct} values (ΔR_{ct}) before and after a new adhesive layer preparation was considered as the main response. By comparing two kinds of aptasensors, the ΔR_{ct} value caused by the pristine CuCo PBA is the largest, 0.83 kohm, suggesting its

poor electrochemical activity. On the contrary, the AuNP@CuCoPBA/AE exhibits the smallest R_{ct} value, indicating the addition of the AuNPs can enhance electrochemical conductivity and boost the electron transfer at the interface of the electrode and electrolyte solution. When immobilizing the aptamer strands, the largest ΔR_{ct} value is observed for the Apt/AuNP@CuCoPBA/AE, 0.21 kohm, but only slightly higher than that of the Apt/CuCoPBA/AE (0.19 kohm). Therefore, the presence of the AuNPs not only can improve the electrochemical activity but also can strengthen the aptamer immobilization. The immobilization of aptamer strands over the AuNP@CoCuPBA is attributed to the complex interaction, including covalent valence bonds between Au atoms and the amino groups of aptamer via the formation of the Au-N bonds [23], and coordination forces between the metallic ions centers and the aptamer strands [24]. Additionally, owning to the intrinsic cavities of the CoCu PBA, the aptamer strands not only can be immobilized onto the composite surface but also can penetrate into the PBA interior and be anchored [14]. After the detection of OTA, the Apt/AuNP@CuCoPBA/AE exhibits the largest ΔR_{ct} value, 0.25 kohm, while the Apt/CuCoPBA/AE only has a very small ΔR_{ct} change, 0.075 kohm. The transformation of aptamer conformation to G-quadruplex structure upon OTA/aptamer binding hindered the diffusion of $[Fe(CN)_6]^{3-/4-}$ at the electrode interface, which further resulted in an increased R_{ct} value [5]. It is obvious for that although the CuCoPBA/AE and AuNP@CuCoPBA/AE possess comparable aptamer immobilization, the Apt/AuNP@CuCoPBA/AE shows a superior detection ability for OTA. These results hint that the formed G-quadruplex between the aptamer strands and OTA can be easily removed from the CuCo PBA substrate, leading to a small change in the EIS response.

Given the substantial difference among various nanomaterials, direct evaluation of their detection efficiency toward the same analyte is difficult. In order to eliminate the deviation effect caused by the pristine CuCo PBA and AuNP@CuCoPBA, a relative change in R_{ct} values $[(R_{ct,i+1}\text{-}R_{ct,i})/R_{ct,i}]$ caused by the aptamer immobilization and OTA detection using different aptasensors were used to analyze their sensing performances. As displayed in Fig. 3d, the aptamer immobilization ability of the AuNP@CuCoPBA/AE is 3.5-fold that of the CuCoPBA/AE, whereas the OTA detection ability of the AuNP@CuCoPBA-based aptasensor is 7.54-fold that of the CuCoPBA-based aptasensor. These results reveal that the AuNP@CuCoPBA-based aptasensor displays an outstanding aptamer binding ability and high stabilization ability of the formed G-quadruplex. Based on the analyses of the basic characterizations of AuNP@CuCoPBA, the excellent electrochemical biosensing feature of the AuNP@CuCoPBA-based aptasensor is mainly due to the following four aspects: (i) an outstanding ability to mediate fast electron-transfer kinetics of AuNPs endows the aptasensor with fast response time [25]; (ii) significantly extended active surface area with high porosity and robust structure of PBAs [26]; and (iii) favorably tuned electronic structure by combining active transition metals [27]. All of these advantages can facilitate the aptamer strand immobilization and adsorption of analytes. Additionally, to assess the quantities of AuNP@CuCoPBA on the sensing performance, the AuNP@CuCoPBA suspensions with different concentrations of 1, 2, 3, 4, 5, 7, and 9 μg mL^{-1} were deposited on the bare AE to fabricate aptasensors for detecting OTA, which was determined by EIS (**Fig. S7**). The caused ΔR_{ct} by the detection of OTA increased with increasing the AuNP@CuCoPBA concentration at first. When the AuNP@CuCoPBA concentration was higher than 4 μg mL^{-1}, the caused ΔR_{ct} was approached to a level-off. Moreover, too thick AuNP@CuCoPBA layer can make it to remove from the AE surface. Therefore, the AuNP@CuCoPBA suspension with the concentration of 4 μg mL^{-1} is optimal for detecting OTA in this work, and it was used all-through whole electrochemical measurements during the OTA detection.

Sensing performances of the AuNP@*CuCoPBA*-based aptasensor

The detection limit, selectivity, reproducibility, stability, and repeatability of the AuNP@CuCoPBA-based aptasensor were investigated to assess it sensing quality for the detection of OTA. Figure 4a illustrates the Nyquist plots of the AuNP@CuCoPBA-based aptasensor incubated in OTA solutions with different concentrations. This result demonstrates that R_{ct} values increase with increasing OTA concentration. A linear relationship between ΔR_{ct} ($\Delta R_{ct} = R_{ct,\ OTA\ detection} - R_{ct,\ aptamer\ immobilization}$) and OTA concentration is illustrated in Fig. 4b, along with a wide linear range from 50.0 fg mL^{-1} to 10.0 ng mL^{-1}. The linear regression can be represented by ΔR_{ct} (kohm) = 0.33 $\log C_{OTA}$ + 0.47 with a correlation of $R^2 = 0.9931$. The detected and quantified lowest concentration is known as the limitation of detection (LOD) and is calculated by using the equations $3S_{blank}/m$ [5], in which S_{blank} and m illustrate the signal of blank sample and the slope, respectively. The calculated LOD was 5.2 fg mL^{-1} toward OTA. Compared with another reported OTA aptasensors, the AuNP@CuCoPBA-based one displays a low LOD toward OTA (Table 1). This finding may be resulted from the advantages of the fabricated nanomaterials, such as large surface area, fast response kinetics for detecting OTA, and strong adsorption ability of the cavities PBA matrix.

To probe the selectivity of the OTA aptasensor based on AuNP@CuCoPBA nanospheres, other antibiotics, including bbleomycin (BLM), ampicilin (AMP), tobramycin (TOB), streptomycin sulfate (RFP), doxorubicin hydrochloride (ADR), and aflatoxin (AFB1), were used as possible

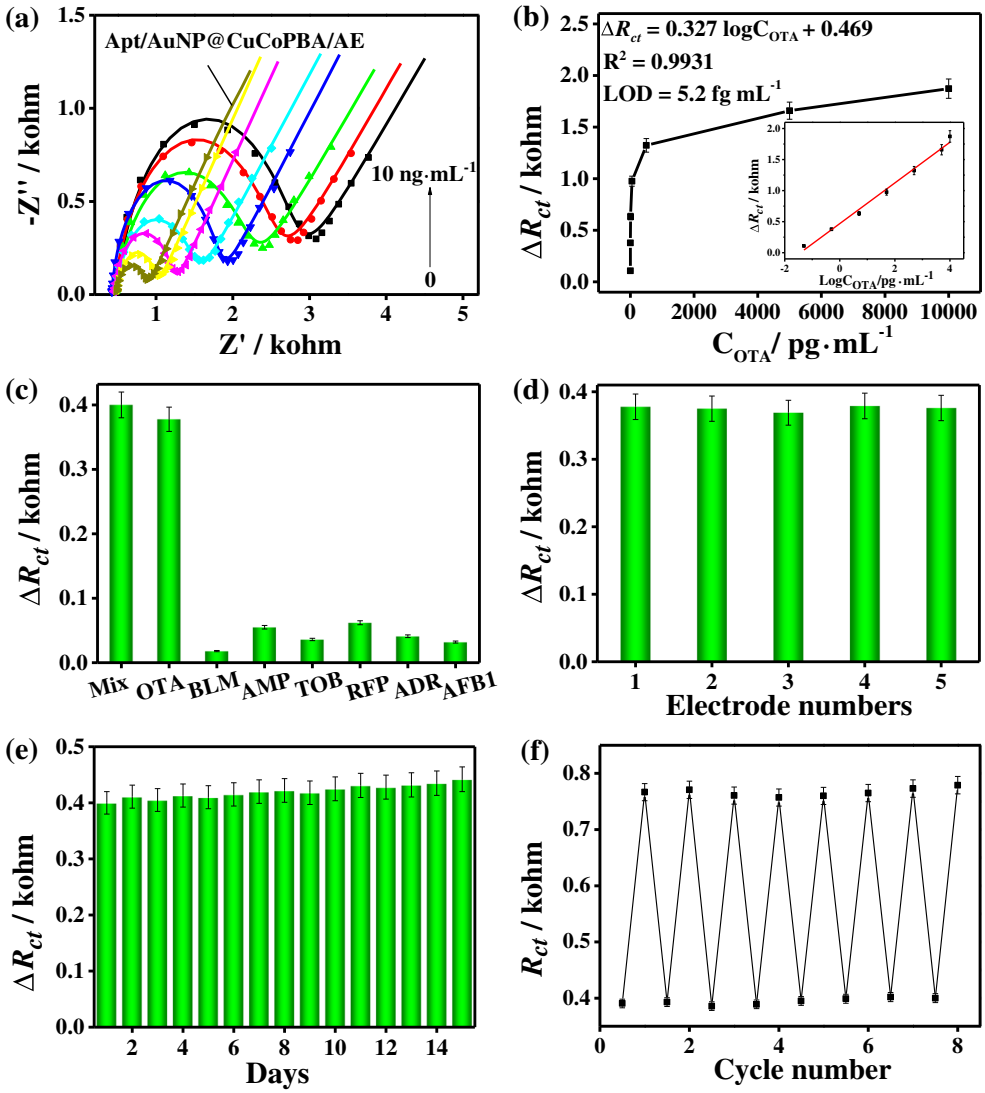

Fig. 4 **a** EIS responses of the Apt/AuNP@CuCoPBA/AE with different OTA concentrations (0.05, 0.5, 5, 50, 500, 5000, 10,000 pg mL^{-1}); (b) Dependence of ΔR_{ct} on the concentration of OTA based on the Apt/AuNP@CuCoPBA/AE. The linear parts of the calibration plots are shown in the inset of **b**. For the sensing selectivity measurement, **c** ΔR_{ct} values of the electrochemical aptasensors by separately adding the interferents (BLM, AMP, TOB, RFP, ADR, and AFB1 with the concentration of 50.0 pg mL^{-1}), OTA (0.5 pg mL^{-1}), and their mixture. **d** Reproducibility, **e** stability, and **f** regeneration of the AuNP@CuCoPBA-based electrochemical biosensor for the detection of OTA (0.5 pg mL^{-1})

interferences with a concentration 100-fold that of OTA solution. The ΔR_{ct} values caused by each interferents, mixed solution, and OTA solution are displayed in Fig. 4c. The addition of OTA (0.5 pg mL^{-1}) leads to a clear ΔR_{ct} value, whereas the addition of other interferences (50.0 pg mL^{-1}) only causes negligible signal EIS responses. Moreover, no

Table 1 Comparison with other published work for detection of OTA

Materials	Methods	Detection range (pg mL^{-1})	LOD (pg mL^{-1})	Refs
Fe_3O_4@Au MBs	Fluorescence	2–5 × 10^3	0.67	[28]
g-CNNS	CV	0.2–500 nM	0.073 nM	[29]
Gold nanorods (GNRs)	localized surface plasmon resonance	10 pM–100 nM	12.0 pM	[17]
porous silicon (PSi)	Photoluminescence (PL)	1–1 × 10^5	4.4	[30]
. Paramagnetic microparticle beads (MBs)	Differential pulse voltammetry (DPV)	780–8740	70	[31]
scaffolded silver-nanocluster (AgNCs)	Fluorescence and UV–vis measurement	10–300	2	[32]
$CSiO_2$NPs	Chemiluminescence (CL)	1–5 × 10^4	0.3	[33]
2D MoS_2	i-t curve	0.5–1 × 10^3	0.23	[34]
aptamer/DNA duplex	DPV	5–1 × 10^5	2	[35]
AuNP@CuCoPBA	EIS	0.05–1 × 10^4	5.2 × 10^{-3}	This work

substantial change in the R_{ct} value was obtained in the mixed solution of interferences in comparison with OTA. Consequently, these results indicate that the aptasensor exhibits a satisfactory selectivity.

Reproducibility is an important property in biosensing technology. The equally five electrodes were used to assess the repeatability of the aptasensor for detecting OTA (0.5 pg mL^{-1}) under the same conditions (Fig. 4d). The average value and standard deviation were calculated to be 375.4 pg mL^{-1} and 3.88%, respectively. In addition, the storage stability is another important parameter for clinical applicability of the aptasensors. To investigate the storage stability of the fabricated biosensor, the modified AE electrode was stored at 4 °C (in dry form) for 15 days (Fig. 4e). EIS responses were measured every day. The AuNP@CuCoPBA-based aptasensor exhibits good sensing performance for 15 days, suggesting excellent stability. Moreover, the regeneration ability is an indicator of biosensor success. Herein, the AuNP@CuCoPBA-based aptasensor was dipped in 0.5 M KOH solution for 5 min. and then incubated in PBS solution containing OTA. Substantial EIS responses were recovered. The same procedure was repeated for 15 cycles (Fig. 4f). Thus, the aptasensor has excellent OTA sensing performance, including selectivity, reproducibility, stability, and repeatability.

Practicability of the aptasensor toward OTA

To validate the applicability of the AuNP@CuCoPBA-based aptasensor in real samples, the OTA solution with different concentrations of 0.05, 0.5, 5, 50, 500, and 5000 fg mL^{-1} was spiked into a fruit juice. EIS responses were collected as corresponding binding signals. The AuNP@CuCoPBA-based aptasensor was washed for another 30 s to completely remove the physically adsorbed molecules. The concentration was calculated using the calibration plot in the inset of Fig. 4b. Afterwards, the recovery rates and relative standard deviations (RSDs) were obtained, as summarized in **Table S2**. The recovery rates of all samples were found to be between 93.55%–104.9%, along with an RSD of less than 4.8%, suggesting high accuracy and repeatability of the fabricated aptasensor.

Conclusion

We have synthesized the nanocomposite of CuCo PBA nanospheres embedded with Au NPs to improve the electrochemical activity and aptamer binding force, following by using it to construct a novel aptasensor for sensitively detecting harmful molecules. Although the presence of Au NPs does not influence the chemical component and crystal structure, it can enhance the electrochemical activity, further improving the sensing performance toward the analyte through the binding of the corresponding aptamer probe. Electrochemical results revealed that the AuNP@CuCoPBA nanospheres demonstrated superior detection efficiency toward OTA, which is mainly attributed to an outstanding ability to mediate fast electron-transfer kinetics of Au NPs and strong affinity for binding aptamer strands. Consequently, the AuNP@CuCoPBA-based aptasensors not only possessed ultrasensitively low LOD toward OTA but also showed high selectivity, long term stability, excellent reproducibility, and long remarkable acceptability. This work provides a new approach to fabricate new aptasensors using the PBA materials for the detection of other analytes.

Acknowledgements This work was supported by Programs for the National Natural Science Foundation of China, China (NSFC: Account Nos. 81601082, 81371363, and U1604127) and Innovative Technology Team of Henan Province, China (CXTD2014042).

Compliance with ethical standards The author(s) declare that they have no competing interests.

References

1. Oršolić N, Jazvinšćak Jembrek M, Terzić S (2017) Honey and quercetin reduce ochratoxin A-induced DNA damage in the liver and the kidney through the modulation of intestinal microflora. Food Agr Immunol 28:812–833
2. Quintela S, Villarán MC, López De Armentia I, Elejalde E (2013) Ochratoxin a removal in wine: a review. Food Control 30:439–445
3. Jiang C, Lan L, Yao Y, Zhao F, Ping J (2018) Recent progress in application of nanomaterial-enabled biosensors for ochratoxin a detection. TrAC Trend Anal Chem 102:236–249
4. Bougrini M, Baraket A, Jamshaid T, Aissari AE, Bausells J, Zabala M, Bari NE, Bouchikhi B, Jaffrezic-Renault N, Abdelhamid E, Zine N (2016) Development of a novel capacitance electrochemical biosensor based on silicon nitride for ochratoxin a detection. Sensor Actuat B-Chem 234:446–452
5. Zhang Z, Ji H, Song Y, Zhang S, Wang M, Jia C, Tian J, He L, Zhang X, Liu C (2017) Fe(III)-based metal-organic framework-derived core-shell nanostructure: sensitive electrochemical platform for high trace determination of heavy metal ions. Biosens Bioelectron 94:358–364
6. Sakurai K, Snyder TM, Liu DR (2005) DNA-templated functional group transformations enable sequence-programmed synthesis using small-molecule reagents. J Am Chem Soc 127:1660–1661
7. Beiranvand ZS, Abbasi AR, Dehdashtian S, Karimi Z, Azadbakht A (2017) Aptamer-based electrochemical biosensor by using au-Pt nanoparticles, carbon nanotubes and acriflavine platform. Anal Biochem 518:35–45
8. Bi S, Li L, Zhang S (2010) Triggered polycatenated DNA scaffolds for DNA sensors and aptasensors by a combination of rolling circle amplification and DNAzyme amplification. Anal Chem 82:9447–9454
9. Zakaria MB, Chikyow T (2017) Recent advances in prussian blue and prussian blue analogues: synthesis and thermal treatments. Coordin Chem Rev 352:328–345
10. Chu Z, Liu Y, Jin W (2017) Recent progress in prussian blue films: methods used to control regular nanostructures for electrochemical biosensing applications. Biosens Bioelectron 96:17–25

11. Zhao J, Liu J, Tricard S, Wang L, Liang Y, Cao L, Fang J, Shen W (2015) Amperometric detection of hydrazine utilizing synergistic action of prussian blue@silver nanoparticles/graphite felt modified electrode. Electrochim Acta 171:121–127
12. Sgobbi LF, Razzino CA, Machado SAS (2016) A disposable electrochemical sensor for simultaneous detection of sulfamethoxazole and trimethoprim antibiotics in urine based on multiwalled nanotubes decorated with prussian blue nanocubes modified screen-printed electrode. Electrochim Acta 191:1010–1017
13. Xu X, Liang H, Ming F, Qi Z, Xie Y, Wang Z (2017) Prussian blue analogues derived penroseite (Ni,co)Se_2 nanocages anchored on 3D graphene aerogel for efficient water splitting. ACS Catal 7:6394–6399
14. Wang M, Yang L, Hu B, Liu J, He L, Jia Q, Song Y, Zhang Z (2018) Bimetallic NiFe oxide structures derived from hollow NiFe Prussian blue nanobox for label-free electrochemical biosensing adenosine triphosphate. Biosens Bioelectron 113:16–24
15. Xin W, Severino J, De Rosa IM, Yu D, Mckay J, Ye P, Yin X, Yang J, Carlson L, Kodambaka S (2018) One-step synthesis of tunable-size gold nanoplates on graphene multilayers. Nano Lett 18:1875–1881
16. Delville A (2005) Influence of confinement on the electrostatic interaction between charged colloids: a (N, V, T) Monte Carlo study within hyperspherical geometry. J Phys Chem B 109:8164–8170
17. Lee B, Park J, Byun J, Kim JH, Kim M (2018) An optical fiber-based LSPR aptasensor for simple and rapid in-situ detection of ochratoxin a. Biosens Bioelectron 102:504–509
18. Park J, Byun J, Jang H, Hong D, Kim M (2017) A highly sensitive and widely adaptable plasmonic aptasensor using berberine for small-molecule detection. Biosens Bioelectron 97:292–298
19. Yang Y, Sangeetha P, Chen Y (2009) Au/FeO_x-TiO_2 catalysts for the preferential oxidation of CO in a H_2 stream. Ind Eng Chem Res 48:10402–10407
20. Xu Z, Hou Y, Sun S (2007) Magnetic Core/Shell Fe_3O_4/au and Fe_3O_4/au/ag nanoparticles with tunable plasmonic properties. J Am Chem Soc 129:8698–8699
21. Chen JR, Jiao XX, Luo HQ, Li NB (2013) Probe-label-free electrochemical aptasensor based on methylene blue-anchored graphene oxide amplification. J Mater Chem B 1:861–864
22. Rivas, L, Mayorga-Martinez, CC, Quesada-González, D, Zamora-Gálvez, A, de la Escosura-Muñiz, A, Merkoçi, A, (2015) Label-free impedimetric aptasensor for ochratoxin-a detection using iridium oxide nanoparticles. Anal Chem 87:5167–5172
23. Ma M, Zhuo Y, Yuan R, Chai Y (2015) New signal amplification strategy using semicarbazide as co-reaction accelerator for highly sensitive electrochemiluminescent aptasensor construction. Anal Chem 87:11389–11397
24. Shanbhag BK, Liu C, Haritos VS, He L (2018) Understanding the interplay between self-assembling peptides and solution ions for tunable protein nanoparticle formation. ACS Nano 12:6956–6967
25. Lawal AT (2018) Progress in utilisation of graphene for electrochemical biosensors. Biosens Bioelectron 106:149–178
26. Shang Z, Chen Z, Zhang Z, Yu J, Tan S, Ciucci F, Shao Z, Lei H, Chen D (2018) CoFe nanoalloy particles encapsulated in nitrogen-doped carbon layers as bifunctional oxygen catalyst derived from a prussian blue analogue. J Alloy Compd 740:743–753
27. Ahn W, Park MG, Lee DU, Seo MH, Jiang G, Cano ZP, Hassan FM, Chen Z (2018) Hollow multivoid nanocuboids derived from ternary Ni-co-Fe prussian blue analog for dual-electrocatalysis of oxygen and hydrogen evolution reactions. Adv Funct Mater 28:1802129
28. Qian J, Ren C, Wang C, Chen W, Lu X, Li H, Liu Q, Hao N, Li H, Wang K (2018) Magnetically controlled fluorescence aptasensor for simultaneous determination of ochratoxin a and aflatoxin B1. Anal Chim Acta 1019:119–127
29. Zhu X, Kou F, Xu H, Han Y, Yang G, Huang X, Chen W, Chi Y, Lin Z (2018) Label-free ochratoxin a electrochemical aptasensor based on target-induced noncovalent assembly of peroxidase-like graphitic carbon nitride nanosheet. Sensor Actuat B-Chem 270:263–269
30. Myndrul V, Viter R, Savchuk M, Shpyrka N, Erts D, Jevdokimovs D, Silamiķelis V, Smyntyna V, Ramanavicius A, Iatsunskyi I (2018) Porous silicon-based photoluminescence immunosensor for rapid and highly-sensitive detection of ochratoxin a. Biosens Bioelectron 102:661–667
31. Bonel L, Vidal JC, Duato P, Castillo JR (2011) An electrochemical competitive biosensor for ochratoxin a based on a DNA biotinylated aptamer. Biosens Bioelectron 26:3254–3259
32. Chen J, Zhang X, Cai S, Wu D, Chen M, Wang S, Zhang J (2014) A fluorescent aptasensor based on DNA-scaffolded silver-nanocluster for ochratoxin a detection. Biosens Bioelectron 57:226–231
33. Hun X, Liu F, Mei Z, Ma L, Wang Z, Luo X (2013) Signal amplified strategy based on target-induced strand release coupling cleavage of nicking endonuclease for the ultrasensitive detection of ochratoxin a. Biosens Bioelectron 39:145–151
34. Tang J, Huang Y, Cheng Y, Huang L, Zhuang J, Tang D (2018) Two-dimensional MoS_2 as a nano-binder for ssDNA: ultrasensitive aptamer based amperometric detection of ochratoxin a. Microchim Acta 185:162
35. Qing Y, Li X, Chen S, Zhou X, Luo M, Xu X, Li C, Qiu J (2017) Differential pulse voltammetric ochratoxin a assay based on the use of an aptamer and hybridization chain reaction. Microchim Acta 184:863–870